Evolution of moisture transport properties in cement mortar under marine salt spray environment

npj | heritage science

Article

https://doi.org/10.1038/s40494-026-02562-z

Evolution of moisture transport properties in cement mortar under marine salt spray environment

Check for updates

Bing Li[1] ✉, Xiyang Dai[1], Simin He[1], Saierjiang Halike[1] ✉, Feng Shi[2], Jean-Marc Tulliani[3], Junsong Wang[4] & Qinglin Meng[4]

Chronic marine salt spray exposure critically alters pore structure and hygrothermal performance of historic building materials. This study investigates the humidity-dependent water vapor permeability (δ_v) of cement mortar with salt deposition. Using accelerated salt spray testing (35 cycles) and cup tests across humidity gradients, cement mortar exhibited opposing δ_v responses: a reduction of 1.86×10^{-12} kg/(m s Pa) under low humidity from pore blockage, and an increase of 1.98×10^{-11} kg/(m s Pa) at high humidity from brine migration. A predictive piecewise model ($R^2 > 0.95$) incorporating salt content and ambient humidity thresholds was developed. MIP and SEM analyses revealed NaCl crystallization preferentially occupying 0.02–0.12 μm pores within the top 2 mm, reducing porosity by 42% while creating dual transport modes: pore occlusion (dry) and interconnected brine networks (humid). These findings provide a framework for predicting moisture dynamics in porous materials under salt spray climates, enabling improved hygrothermal simulations for coastal historic buildings.

An axiom in Chinese heritage conservation holds that "dry conditions preserve for millennia, constantly wet conditions for centuries, but alternating dry–wet conditions cause decay within years." In natural environments, building materials are subjected to long-term cyclic hygrothermal loads, during which moisture undergoes repeated migration, storage, and phase change within porous structures[1–3]. These processes often lead to structural damage—such as cracking, strength loss, surface weathering, color fading, and biological growth—in historic buildings[4–9]. Accurate prediction and quantification of moisture transport in porous materials are therefore essential for enhancing the resilience and durability of built heritage. Coastal regions, which cover ~18.43% of the world's land area, are home to about 52.8% of the global population[9]. Benefiting from well-developed transportation, communication, infrastructure, and economic activity[10–12], coastal and island cities also concentrate a significant portion of the world's cultural heritage and historic architecture[13–16]. In these environments, long-term exposure to marine salt spray induces salt crystallization in conventional building materials such as brick, mortar, and plaster, fundamentally altering pore structures and disrupting moisture transport mechanisms[17–19]. Under cyclic moisture and salt action, coupled heat and moisture transport occurs within porous materials, significantly affecting their physical properties and functional performance, thereby posing considerable challenges to building envelopes[2,17,20–22]. A thorough investigation and systematic interpretation of these processes are essential for advancing conservation techniques and sustainable management strategies for coastal historic structures.

The deposition of salt crystals alters the original pore characteristics of porous materials by occupying their pore volume. Recent studies have elucidated the mechanisms of salt crystallization and growth within porous building materials. Systematic laboratory analyses of common construction materials—including brick[23], sandstone[24], limestone[3], plaster[25], and mortar[26]— confirm that salt deposition fundamentally alters porosity and pore architecture. The two most commonly used salts in experiments are Na_2SO_4 and NaCl. Mercury intrusion porosimetry (MIP) data indicate that Na_2SO_4 reduces porosity by 6–8%[19,23,27], whereas NaCl can lead to more substantial reductions, with reported values ranging from 4% to 10%[25,28] up to 47–50% under specific conditions[19,27]. Collectively, these studies reveal a general trend of porosity reduction due to salt crystallization. However, substantial inconsistencies persist across experimental results, which may arise from variable factors including salt speciation (e.g., crystalline polymorphism), solution molarity, salt exposure protocol, sampling location, and material-specific pore heterogeneity[3,18,19,24,25,29]. The combined effects of saline environments and multiple factors result in distinct pore distribution

[1]College of Civil Engineering and Architecture, Xinjiang University, Urumqi, China. [2]College of Horticulture and Forestry, Tarim University, Alar, China. [3]Department of Applied Science and Technology, Politecnico di Torino, Torino, Italy. [4]State Key Laboratory of Subtropical Building and Urban Science, South China University of Technology, Guangzhou, China. ✉e-mail: libing@xju.edu.cn; saierjiang@xju.edu.cn

Table 1 | Chemical composition (wt%) of cement CEM II/BL-L 32.5R determined by XRF analysis

Component	CaO	MgO	SO_3	Al_2O_3	Fe_2O_3	K_2O	Na_2O	TiO_2	SrO	P_2O_5	LOI	Others
Content	60.2	3.56	3.46	3.12	2.19	1.12	1.05	0.185	0.147	0.104	12.8	0.19

characteristics in porous materials, thereby altering their inherent moisture transport behavior.

In porous building materials, salt crystallization and moisture transport constitute a dynamically coupled process. Salt crystallization within pores alters the hygric parameters of porous building materials—such as capillary absorption coefficients, capillary moisture retention, and vapor permeability coefficients—through the dual mechanisms of pore occlusion and impaired pore connectivity[18,19,30,31]. Conversely, as salt can only migrate in dissolved form through the pore network, its redistribution is intrinsically moisture-dependent, establishing a mutually causal relationship between moisture transport pathways and salt deposition patterns[29,30,32–34]. This bidirectional coupling introduces unique challenges in coastal saline environments, where dynamic pore-scale interactions between moisture flux and salt crystallization give rise to emergent system-level behavior. Further complicating the issue, methodological variations across studies—stemming from differing research objectives and experimental protocols—have hindered consensus on the evolution of hygric properties in salt-affected porous materials[3,18,19,27,29,34–36]. Consequently, current understanding remains fragmentary, highlighting the necessity of a unified theoretical framework to reconcile experimental inconsistencies and reliably predict material performance in salt-rich environments.

Cement mortar is a porous building material widely used for the masonry, leveling, and plastering of building envelopes. Compared with traditional lime mortar, formulated cement mortar offers superior strength, corrosion resistance, and durability, making it particularly suitable as a masonry and rendering material for the numerous historic buildings and industrial heritage sites in coastal cities that are chronically exposed to salt spray environments[17,37,38]. Despite its extensive application, the moisture transport processes and hygric property parameters of cement mortar under salt spray deposition have yet to be systematically understood, leaving hygrothermal simulations and accurate calculations for building envelopes in coastal saline climates without a sufficient scientific basis. In light of these attributes, our preliminary semi-immersion experiments focused on moisture transport mechanisms in porous building materials under coastal climates, revealing critical relationships between chloride migration and crystallization patterns in cement mortar[30]. The study demonstrated that surface salt crystallization morphology is governed by water-to-cement ratio (W/C)-controlled porosity, while chloride ion distribution along horizontal windward and vertical orientations is indirectly influenced by surface evaporation conditions. Notably, Salt crystallization deposition reduced the capillary absorption coefficient (A_{cap}) by 46% and capillary moisture content (w_{cap}) by 56% in specimens with W/C = 0.6[30]. To better simulate persistent salt spray exposure in coastal regions, we conducted extensive preliminary investigations and parametric optimizations of the salt spray test method to more accurately replicate coastal climatic conditions. Following this, five sets of accelerated salt spray tests were performed on cement mortar specimens. After 35 cycles, these tests showed a chloride concentration of 1.99%, an apparent density increase of 3.85%, reductions of 18.7% in both open porosity (P_0) and saturation moisture content (w_{sat}), as well as decreases of 30% in A_{cap} and 17.4% in w_{cap}[31]. Through parametric analysis of salinity effects on capillary absorption, we established modified computational equations for A_{cap} and w_{cap} in cement mortar under salt spray deposition[31]. This series of systematic studies provides comprehensive insights into the liquid water transport and storage behavior of cement mortar in coastal saline environments.

Building on previous research, this study systematically investigates the effect of salt deposition on water vapor transport in cement mortar through a multi-scale experimental framework. By combining accelerated salt spray tests with gravimetric analysis, we quantified the influence of NaCl deposition on vapor permeability using dry-cup and wet-cup methods under different humidity conditions. Through comparison with salt-free reference specimens, we established a normalized influence factor for the water-vapor permeability coefficient, enabling mathematical modeling of the relationship between permeability and salt content. Microstructural analyses using mercury intrusion porosimetry (MIP) tracked pore evolution over 35 salt-spray cycles, while scanning electron microscopy (SEM) with depth-resolved sampling revealed spatial salt crystallization patterns from the surface to the interior. This integrated multi-scale methodology bridges microscale salt-pore interactions and macroscale moisture-transport phenomena, providing a basis for predicting the hygrothermal performance and structural resilience of historic buildings in coastal salt-spray environments.

Methods

Specimen preparation

Cement mortar was prepared using CEM II/B-LL 32.5R cement (Buzzi, Italy), CEN-standard sand (UNI EN 196-1:2011), and deionized water. The binder composition complied with EN 197-1, consisting of 65–79% clinker, 21–35% limestone, and 0–5% gypsum. The chemical composition of the cement, determined by X-ray fluorescence spectrometry (XRF; Rigaku NEX CG), is provided in Table 1, loss on ignition (LOI) was measured via thermogravimetric-differential thermal analysis (TG-DTA). Constituents were mixed at a mass ratio of 1:3:0.5 (cement: sand: water), homogenized, and cast into $70 \times 70 \times 70\ mm^3$ molds under vibratory compaction. After initial curing at 23 °C and 95% RH for 24 h, specimens were demolded and subsequently water-cured for 28 days at 23 °C under laboratory ambient conditions.

For water vapor permeability evaluation, plate specimens measuring $70 \times 70 \times 20\ mm^3$ were precision-cut from the cured cubes using a diamond saw (Fig. 1(1-1a))). All surfaces were then cleaned sequentially with compressed air and deionized water to remove residual particulates and ensure open pore networks. After cleaning, the specimens were dried, labeled, and grouped for subsequent testing. The selected thickness of 20 mm follows the ISO 12572:2016 specification for homogeneous materials[39], and also aligns well with the typical thickness of cement-based renders, plasters, and repair layers commonly found in historic building envelopes.

Accelerated salt spray cycling test

Salt deposition and corrosion in building materials constitute a long-term process influenced by numerous uncontrollable climatic variables, making field experiments particularly challenging. To investigate moisture transport characteristics of porous building materials under coastal salt-fog conditions, this study employed accelerated salt-spray testing to simulate realistic exposure environments. While existing international salt spray test standards for building materials—such as BS EN 14147:2003(E)[40] and ASTM B117-11(E)[41]—are applicable to natural stone and primarily focus on durability assessment, this study referenced the fundamental test procedures specified in these standards and made corresponding adjustments to experimental parameters based on research objectives.

The experiment was conducted in a CEAST 5050 chamber (Italy), which generated salt fog using a 5 wt% NaCl solution (Fig. 1(1-2, 1-4)). Specimens were mounted at a 20° inclination from the vertical with 44 mm spacing between units (Fig. 1(1-3)). Each test cycle consisted of 8 h of spraying (35 °C, 100% RH) followed by 16 h of drying (55 °C), achieving a salt deposition rate of 2 mL/ (80 cm^2 h) in accordance with ASTM B117-11. This wet-dry cycling improves simulation accuracy by mimicking natural environmental fluctuations. A total of 24 specimens were divided into six groups (5O, 5A–5E) corresponding to 0, 7, 14, 21,28 and 35 exposure cycles,

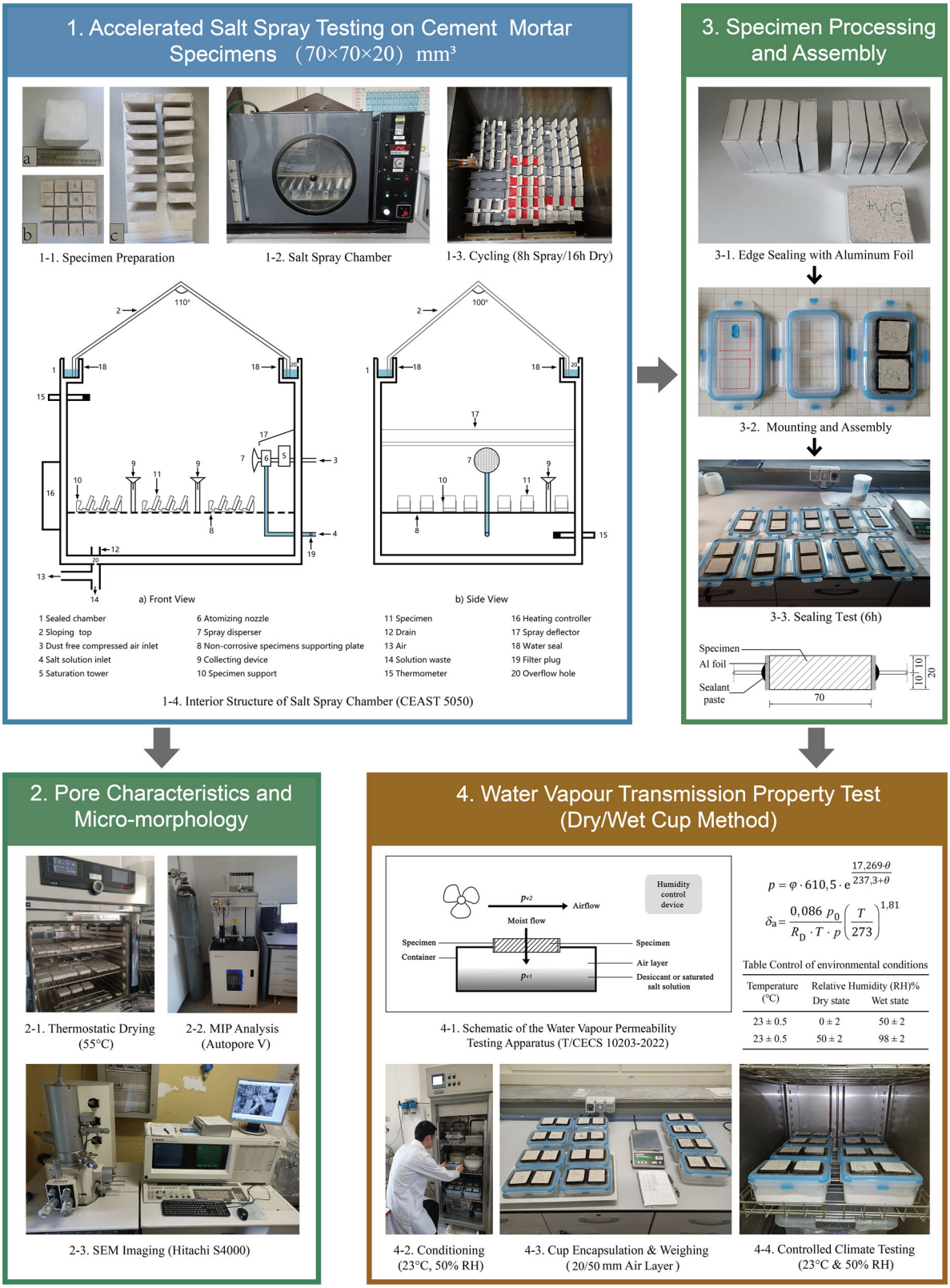

Fig. 1 | Schematic of the experimental setup and protocol for water vapor permeability testing. The figure is composed of four panels arranged chronologically to illustrate the experimental workflow. Panel **1** shows the process and equipment for the accelerated salt spray test, enclosed within a light blue line frame. Panel **2** presents the instruments used for microstructural analysis of the specimens, specifically mercury intrusion porosimetry (MIP) and scanning electron microscopy (SEM), highlighted by a green line frame. Panel **3** depicts the fabrication process of the components for the water vapor permeability test, also indicated by a green line frame. Panel **4** illustrates the setup and procedure for the water vapor permeability test itself (dry-cup and wet-cup methods), enclosed within a brown line frame.

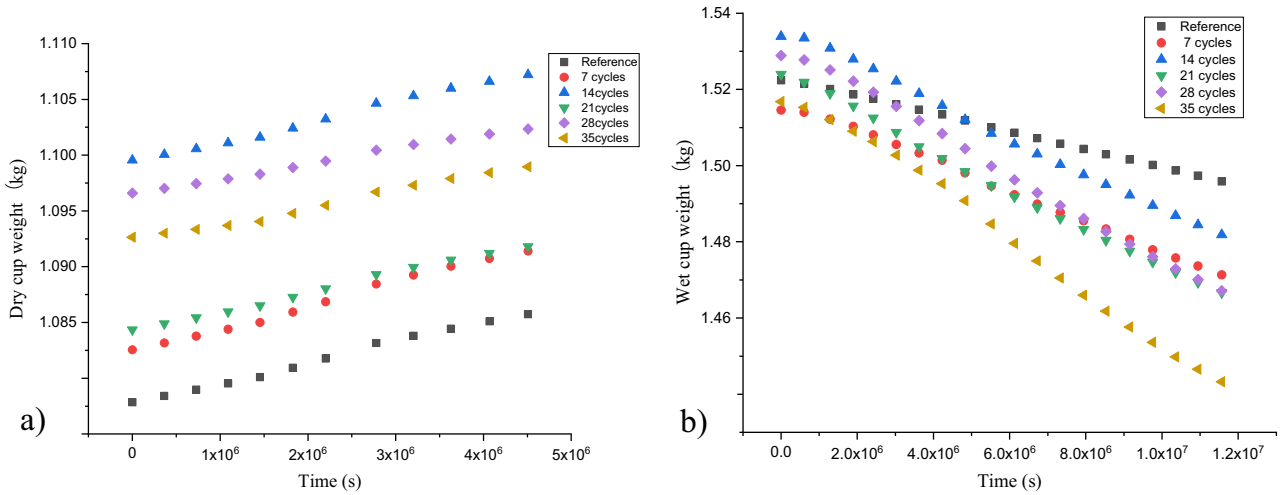

Fig. 2 | Mass variation of dry- and wet-cup specimens during water vapor permeability testing. The figure consists of two panels illustrating the mass change over time for cement mortar specimens subjected to 0–35 salt spray cycles. Panel **a** shows the results from dry-cup tests (0–50% RH gradient), and Panel **b** shows the results from wet-cup tests (50–98% RH gradient). In both panels, the data points are color-coded according to the number of salt spray cycles: black represents the reference specimens (0 cycles); red, 7 cycles; blue, 14 cycles; green, 21 cycles; purple, 28 cycles; and yellow, 35 cycles.

with four replicate specimens per group (e.g., 5A1–5A4). After exposure, all specimens were conditioned at 23 °C and 50% RH until mass stabilization (ISO 12572:2016[39]) to standardize moisture content before permeability testing.

Water vapor permeability measurement

The water vapor permeability of cement mortar was evaluated following ISO 12572: 2016(E)[39] using a custom-designed apparatus (Fig. 1(4-1)) to establish controlled vapor pressure gradients across specimens. Specimens ($70 \times 70 \times 20$ mm³) were edge-sealed with self-adhesive aluminum tape (Fig. 1(3-1)) to prevent sealant penetration into surface pores, then bonded to modified plastic container lids (72×72 mm² openings) using Bostik liquid rubber sealant (Italy). This ensured mid-plane alignment (10 mm exposed above/below the lid) and void-free interfacial contact (Fig. 1(3-2)). Airtightness was verified by submerging specimens in deionized water (2–3 mm below the top surface) for 6 h (Fig. 1(3-3)); any leaking specimens were resealed until integrity was confirmed.

Two test methods were employed to assess moisture transport under varying humidity conditions[39,42]. The dry-cup method simulated low-humidity environments (0 ± 2% RH vs. 50 ± 2% RH, Fig. 1(Table)) using silica gel desiccant, whereas the wet-cup method evaluated high-humidity behavior (50 ± 2% RH vs. 98 ± 2% RH, Fig. 1(Table)) with saturated K_2SO_4 solution maintained with excess salt crystals. Key setup parameters included a 20 mm air layer between specimens and desiccant (dry-cup) and a 50 mm air layer above the solution (wet-cup), with solution depths standardized at 15 mm. All assemblies were preconditioned at 23 ± 0.5 °C and 50 ± 2% RH until mass stabilization (variation <5% over three consecutive days, Fig. 1(4-2)) to ensure uniform moisture distribution prior to permeability testing.

Preconditioned assemblies were sealed onto containers holding an equal mass of desiccant or salt solution (Fig. 1(4-3)) and transferred to a climate-controlled chamber maintained at 23 ± 2 °C and 50 ± 2% RH, with an airflow velocity of ≥100 mm/s. Chamber conditions were verified using Testo 174H sensors (Fig. 1(4-4)). Mass measurements began after 28 days and were performed at 48 h intervals under temperature-controlled conditions (23 ± 2 °C). Weightings continued until the change in mass per interval, determined over five successive measurements for each specimen, remained constant within ±5% of its mean value. This protocol follows the airflow and equilibration requirements of ISO 12572, while incorporating refinements such as airtightness verification and the use of mass-equalized solutions to minimize variability.

The water vapor flux rate G_v (kg/s) through cement mortar specimens was determined via linear regression of the total mass of dry/wet cup assemblies against weighing time, with a coefficient of determination (R^2) ≥ 0.99. The water vapor flow density g_v (kg/m² s¹) was calculated as

$$g_v = \frac{G_v}{A} \tag{1}$$

where A is the exposed surface area of specimen (m²). The vapor pressure difference Δp_v (Pa) across the specimen was derived using:

$$\Delta p_v = p_{v,sat} \cdot |\varphi_1 - \varphi_2| \tag{2}$$

where $p_{v,sat}$ = 2.808 Pa (saturation vapor pressure at 23 °C), and φ_1, φ_2 are relative humidity values on the two sides of the specimen. The total vapor transfer resistance R_{total} (m² s Pa/ kg) was calculated as

$$R_{total} = \frac{p_v}{g_v} \tag{3}$$

The air layer resistance R_{air} (m² s Pa/kg) within the apparatus was determined by:

$$R_{air} = \frac{d_{air}}{\delta_{v,air}} \tag{4}$$

Where d_{air} is the thickness of the air layer (m), and $\delta_{v,air}$ is the water vapor permeability coefficient of static air. The specimen's water vapor permeability coefficient δ_v (kg/ m s Pa) were obtained via:

$$R_{sample} = R_{total} - R_{air} \tag{5}$$

$$\delta_v = \frac{H}{R_{sample}} \tag{6}$$

where R_{sample} is water vapor resistance of specimen (m² s Pa/kg⁻¹). H is the specimen thickness (m).

Microstructural characterization and analysis

The chloride ion content in cement mortar subjected to accelerated salt spray cycles was quantified using a C-CL-3000 electrochemical analyzer (James Instruments, USA). Prior to analysis, the system was calibrated with five Cl^- standard solutions (0.005%, 0.01%, 0.05%, 0.1%, and 0.3%). Full-thickness specimens were ground into powder to assess the depth-

Table 2 | Linear regression analysis of water vapor flow rate (G_v) for cement mortar subjected to salt spray deposition (dry-cup method, 0–50% RH)

Salt spray cycling	Dry cup assembly	G_v (kg/s)	R^2	RSS
Reference	5O1–5O4	2.06783×10^{-9}	0.990	6.00332×10^{-7}
7 Cycles	5A1–5A4	1.82618×10^{-9}	0.992	3.49465×10^{-7}
14 Cycles	5B1–5B4	1.79315×10^{-9}	0.988	5.3501×10^{-7}
21Cycles	5C1–5C4	1.72146×10^{-9}	0.993	2.75475×10^{-7}
28 Cycles	5D1–5D4	1.49543×10^{-9}	0.981	5.83101×10^{-7}
35 Cycles	5D1–5D4	1.32698×10^{-9}	0.993	1.55235×10^{-7}

Table 3 | Linear regression analysis of water vapor flow rate (G_v) for cement mortar subjected to salt spray deposition(wet-cup method, 50–98% RH)

Salt spray cycling	Dry cup assembly	G_v (kg/s)	R^2	RSS
Reference	$5O_1$–$5O_4$	-2.34299×10^{-9}	0.999	6.85676×10^{-7}
7 Cycles	$5A_1$–$5A_4$	-3.94800×10^{-9}	0.997	1.04771×10^{-5}
14 Cycles	$5B_1$–$5B_4$	-4.75102×10^{-9}	0.997	1.42988×10^{-5}
21Cycles	$5C_1$–$5C_4$	-5.09070×10^{-9}	0.998	1.47054×10^{-5}
28 Cycles	$5D_1$–$5D_4$	-5.66033×10^{-9}	0.998	1.75064×10^{-5}
35 Cycles	$5D_1$–$5D_4$	-6.83262×10^{-9}	0.995	5.88554×10^{-5}

dependent distribution of salts. A 3 g aliquot of homogenized powder was dissolved in 20 mL acidic solution, vortexed, and allowed to stabilize for 2 min. After degassing (2–4 min), Cl^- concentrations were determined via potentiometric voltage differentials, with results displayed digitally. All measurements were performed at 23 °C on desiccated specimens, with calibrated batches analyzed within 2 h to minimize instrumental drift.

To establish microstructure-property relationships, mercury intrusion porosimetry (MIP; Autopore V, Micromeritics, USA) and scanning electron microscopy (SEM; S4000, Hitachi, Japan) were utilized (Fig. 1(2-2, 2-3)). SEM samples were prepared as cross-sectional profiles from surface to mid-depth region, dried and sputter-coated with an Au/Pd (SPI Supplies, USA). For MIP, samples were dried at 55 °C to constant mass (Fig. 1(2-2)); then, 3–4 g of each sample was analyzed under a maximum pressure of 2000 MPa, enabling the detection of pores larger than 6 nm in diameter based on the Washburn theory. Two replicates per group ensured statistical validity. All procedures complied with ISO 21466:2019[43] for SEM and ISO 15901-1:2016[44] for MIP, and specimens were kept in anhydrous state throughout pretreatment and handling.

Results and discussion

Dry-cup and wet-cup water vapor permeability coefficient

The mass variations of cement mortar specimens under dry-cup (RH 0/50%) and wet-cup (RH 50%/98%) conditions are illustrated in Fig. 2a, b, respectively. In dry-cup tests (Fig. 2a), the assembly mass increased linearly over time as water vapor was absorbed by the internal silica gel desiccant. Conversely, wet-cup assemblies (Fig. 2b) lost mass linearly due to vapor diffusion from the saturated K_2SO_4 solution to the drier ambient environment. Although minor initial mass differences occurred among the control and salt-sprayed groups (7–35 cycles), resulting from material heterogeneity and slight thickness variations during specimen preparation, they did not affect the validity of mass change rate analyses. Measurement errors across datasets ranged between 0.01% and 0.03%, mainly caused by heterogeneous pore structures and salt crystallization patterns, with negligible influence on the overall results.

Linear regression of mass-time profiles (Fig. 2a, b) provided the water vapor flux rates (G_v) for each assembly (Tables 2 and 3). Dry-cup data showed a coefficient of determination (R^2) > 0.98 and residual sum of squares (RSS) < 6.00×10^{-7}. Notably, the control group exhibited the highest G_v, which decreased progressively with salt spray cycles (Table 2). Wet-cup results demonstrated superior linearity (R^2 > 0.99, RSS < 5.89×10^{-5})), with the control group showing the lowest G_v—a value that increased systematically with more exposure cycles (Table 3).

The water vapor permeability coefficient (δ_v) and associated process parameters for all cement mortar groups were determined using Eq. (1)–(6), with results summarized in Tables 4 and 5. The specimen surface area (A) used for calculating vapor flux density (g_v) was consistent across groups due to mold-controlled dimensions with negligible length/width deviations. To compensate for thickness (H) variations introduced during the cutting process, the reported thickness values represent the average of six measurements taken at different locations using a vernier caliper.

As shown in Table 4 (dry-cup method, 0-50% RH), the control group exhibited the highest vapor permeability coefficient δ_v (5.95×10^{-12} kg/(m s Pa)). This value decreased progressively with increasing salt spray exposure, reaching its lowest level after 35 cycles. In contrast, Table 5 (wet-cup method, 50–98% RH) revealed an opposite trend: the control group displayed a lower baseline δ_v (8.25×10^{-12} kg/(m s Pa)), which increased systematically over 35 exposure cycles. This dichotomy underscores the dual-phase influence of salt crystallization: under low humidity, the pore-blocking effect dominates, reducing δ_v[18,27], whereas under high humidity, deliquescence-induced brine formation enhances moisture transport through liquid-phase action[19,30,45].

Xie et al. [46] reported a water vapor permeability coefficient (δ_v) in the range of 2.66×10^{-12}–4.02×10^{-12} kg/(m s Pa) for cement mortar under 43–97.6% RH, which is slightly lower than the values obtained in this study. This discrepancy likely stems from differences in cement type and mix proportions. Notably, their findings are consistent with the present results: salt deposition suppresses vapor transport under low humidity/high salinity conditions but enhances it under high humidity/elevated salinity environments (Tables 4 and 5, Fig. 3).

The opposing effects of salt deposition on δ_v under different humidity conditions are governed by the deliquescence behavior of NaCl. Below 75% RH (deliquescence threshold at 23 °C[47]), accumulated salt crystals reduce porosity and pore connectivity, increasing vapor transport resistance[19,28,48–50]. Above 75% RH, deliquesced NaCl migrates as brine via wicking and evaporation-driven flows[19,29,30,51]. In the wet-cup configuration, where the low-humidity side is maintained at 50% RH, the brine releases water vapor until recrystallization occurs[18,52], inducing intense liquid-phase mass transport in the porous material that elevates its δ_v. Moreover, the intrinsic hygroscopicity of NaCl further enhances moisture migration as salt content increases.

Salt-induced permeability model

To quantify the effect of salt content on the water vapor permeability coefficient (δ_v) of cement mortar under salt spray exposure, the influence factor η_{δ_v} was calculated for both dry-cup ($\varphi \le 0.75$) and wet-cup ($\varphi > 0.75$) methods using Eq. (7). This parameter integrates the mechanistic influence of NaCl crystallization below 75% RH and deliquescence above 75% RH on vapor transport properties. Polynomial regression was used to express η_{δ_v} as a function of salt content in the low-humidity ($\varphi \le 0.75$) and high-humidity ($\varphi > 0.75$), yielding coefficients of determination (R^2) greater than 0.96 and 0.95, respectively (Fig. 4a, b). This resulting dual-phase model reflects the crystallographic and hygroscopic transitions of NaCl, confirming its role in regulating vapor transport across humidity gradients.

$$\eta_{\delta_v} = \frac{\delta_{v,s}}{\delta_{v,r}} \tag{7}$$

where $\delta_{v,s}$ and $\delta_{v,r}$ are the water vapor permeability coefficients kg/(m s Pa) of salt-containing specimens and salt-free specimens, respectively.

The water vapor permeability coefficient for salt-free porous materials ($\delta_{v,r}$) was derived from Eqs. (1) to (6) and is expressed in Eq. (8). All symbols

Table 4 | Water vapor permeability (δ_v) and process parameters of cement mortar subjected to salt spray deposition (dry cup method, 0–50% RH)

Salt spray cycling	G_v (kg/s)	g_v [kg/(m² s)]	ΔP_v (Pa)	R_{total} (m² s Pa/kg)	R_{air} (m² s Pa/kg)	R_{sample} (m² s Pa/kg)	δ_v [kg/(m s Pa)]	SD
Reference	2.07×10^{-9}	4.22×10^{-7}	1404	3.33×10^{9}	1×10^{8}	3.23×10^{9}	5.95×10^{-12}	2.76×10^{-13}
7 Cycles	1.83×10^{-9}	3.73×10^{-7}	1404	3.77×10^{9}	1×10^{8}	3.67×10^{9}	5.78×10^{-12}	5.51×10^{-13}
14 Cycles	1.79×10^{-9}	3.66×10^{-7}	1404	3.84×10^{9}	1×10^{8}	3.74×10^{9}	5.66×10^{-12}	1.48×10^{-13}
21Cycles	1.72×10^{-9}	3.51×10^{-7}	1404	4.00×10^{9}	1×10^{8}	3.90×10^{9}	5.17×10^{-12}	3.01×10^{-13}
28 Cycles	1.50×10^{-9}	3.05×10^{-7}	1404	4.60×10^{9}	1×10^{8}	4.50×10^{9}	4.54×10^{-12}	1.19×10^{-13}
35 Cycles	1.33×10^{-9}	2.71×10^{-7}	1404	5.18×10^{9}	1×10^{8}	5.08×10^{9}	4.09×10^{-12}	1.35×10^{-13}

Table 5 | Water vapor permeability coefficient (δ_v) and process parameters of cement mortar subjected to salt spray deposition (wet cup method, 50–98% RH)

Salt Spray Cycling	G_v (kg/s)	g_v [kg/(m² s)]	ΔP_v (Pa)	R_{total} (m² s Pa/kg)	R_{air} (m² s Pa/kg)	R_{sample} (m² s Pa/kg)	δ_v [kg/(m s Pa)]	SD
Reference	2.34×10^{-9}	4.78×10^{-7}	1347.84	2.82×10^{9}	2.5×10^{8}	2.57×10^{9}	8.25×10^{-12}	3.94×10^{-13}
7 Cycles	3.95×10^{-9}	8.06×10^{-7}	1347.84	1.67×10^{9}	2.5×10^{8}	1.42×10^{9}	1.40×10^{-11}	7.69×10^{-13}
14 Cycles	4.75×10^{-9}	9.70×10^{-7}	1347.84	1.39×10^{9}	2.5×10^{8}	1.14×10^{9}	1.88×10^{-11}	4.61×10^{-13}
21Cycles	5.28×10^{-9}	1.08×10^{-6}	1347.84	1.25×10^{9}	2.5×10^{8}	1.00×10^{9}	2.10×10^{-11}	1.02×10^{-12}
28 Cycles	5.66×10^{-9}	1.16×10^{-6}	1347.84	1.17×10^{9}	2.5×10^{8}	9.20×10^{8}	2.38×10^{-11}	1.01×10^{-12}
35 Cycles	6.83×10^{-9}	1.39×10^{-6}	1347.84	9.67×10^{8}	2.5×10^{8}	7.17×10^{8}	2.80×10^{-11}	7.83×10^{-13}

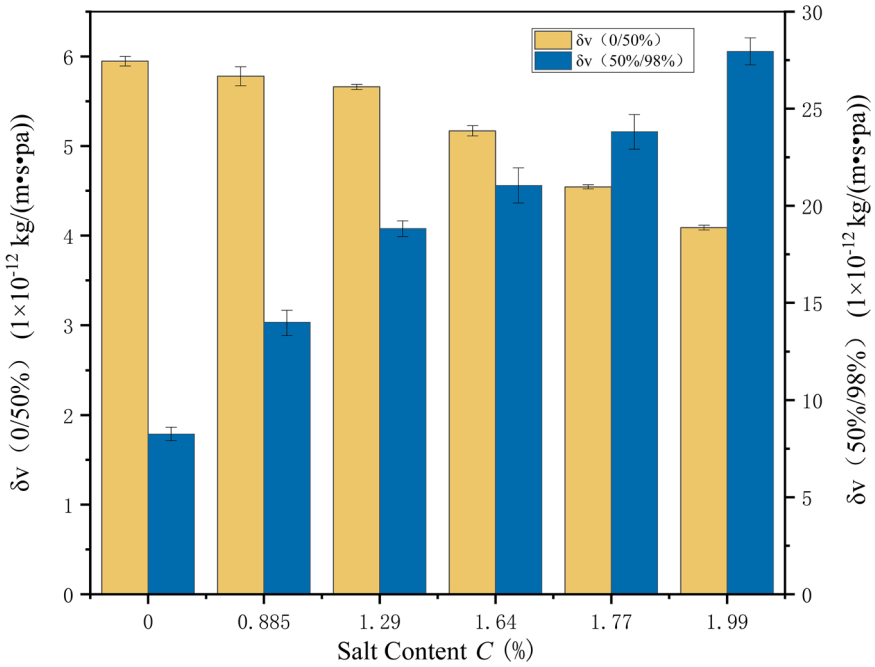

Fig. 3 | Water vapor permeability coefficients versus salt content in cement mortar. The figure presents the measured water vapor permeability coefficients of cement mortar specimens with varying salt contents following salt spray exposure. Yellow bars represent results from dry-cup tests (0–50% RH gradient), corresponding to the left vertical axis, while blue bars represent results from wet-cup tests (50–98% RH gradient), corresponding to the right vertical axis. Error bars indicating the standard deviation are shown atop each bar to illustrate the variability among replicate specimens for each test condition.

and units in this expression are consistent with those defined in the section "Water vapor permeability measurement". To account for the influence of salt deposition, $\delta_{v,r}$ was subsequently modified by applying the polynomial fit for the influence factor η_{δ_v} (Fig. 4), yielding the adjusted permeability coefficient $\delta_{v,s}$ for NaCl- contaminated cement mortar, as expressed in Eq. (9):

$$\delta_{v,r} = \frac{H}{\frac{p_{v,sat}\cdot A\cdot|\varphi_1-\varphi_2|}{G_v} - \frac{d_{air}}{\delta_{v,air}}} \tag{8}$$

$$\delta_{v,s} = \begin{cases} (-2983.71C^2 + 59.12C + 0.68)\dfrac{H}{\frac{p_{v,sat}\cdot A\cdot|\varphi_1-\varphi_2|}{G_v} - \frac{d_{air}}{\delta_{v,air}}} & \varphi_1 \le 0.75\ R^2 = 0.96 \\ (6035.16C^2 - 28.26C + 1.51)\dfrac{H}{\frac{p_{v,sat}\cdot A\cdot|\varphi_1-\varphi_2|}{G_v} - \frac{d_{air}}{\delta_{v,air}}} & \varphi_1 > 0.75\ R^2 = 0.95 \end{cases} \tag{9}$$

Compared with traditional calculation methods, Eq. (9) fully accounts for the influence of salt content on the water vapor permeability of porous materials under salt spray deposition. Through piecewise fitting of the influence factor, it captures the role of salt in vapor transport across different humidity regimes, while also reflecting the underlying microscopic

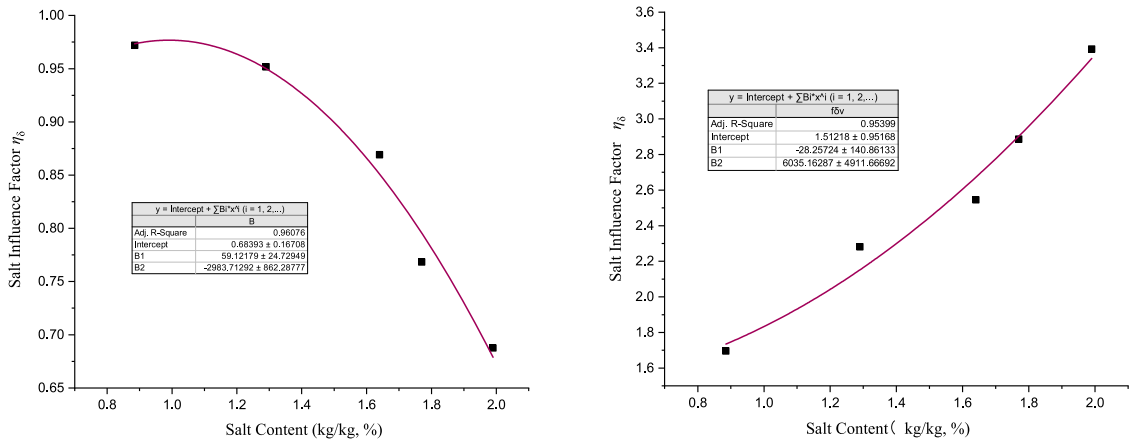

a) $\varphi_1 \leq 0.75$ b) $\varphi_1 > 0.75$

Fig. 4 | Influence factor ($\eta_{\delta v}$) for water vapor permeability as a function of salt content in cement mortar. The figure consists of two panels illustrating the salt influence factor derived from different humidity conditions. Panel **a** shows the influence factor obtained from dry-cup tests (low humidity regime) and the corresponding quadratic fitted curve. Panel **b** shows the influence factor obtained from wet-cup tests (high humidity regime) and its fitted curve. The fitting curves in the two panels exhibit opposite trends, indicating that the effect of salt content on the water vapor permeability coefficient is strongly dependent on ambient humidity.

mechanisms—namely, salt crystallization and deliquescence—that govern water vapor permeability in porous materials. Experimental measurement of δ_v for diverse materials is both labor-intensive and time-consuming. With Eq. (9), the δ_v of common building materials—as documented in existing hygric property databases—can be directly calculated based on a given salt deposition level and ambient humidity, thereby eliminating the need for extensive repeated testing. It should be noted that the proposed piecewise model is formulated based on the external boundary humidity conditions, rather than on the local humidity within the material. Therefore, for steady-state hygrothermal simulations, the appropriate equation can be selected according to the prescribed ambient humidity. For more refined transient simulations involving internal humidity gradients, a multilayer approach that couples the humidity gradient with the salt distribution would be more suitable—an important direction that warrants further investigation.

Pore structure and microscopic morphology

The water vapor permeability of porous building materials is primarily controlled by their pore structure. In cement mortar, salt crystallization within pores represents the key factor altering the permeability coefficient. To investigate the microstructural origins of these changes in salt-containing specimens, this study employed mercury intrusion porosimetry (MIP) to quantify pore parameters, combined with scanning electron microscopy (SEM) for morphological characterization.

To examine microstructural changes in cement mortar under salt spray exposure, pore size distributions of specimens subjected to 7–35 salt spray cycles were systematically compared with those of reference specimens (Fig. 5a–e). The dominant pore volume peak in cement mortar was observed at approximately 0.1 μm. Under cyclic salt spray conditions, pore volumes within the 0.02–0.12 μm range exhibited a progressive decline (16-42%) with increasing exposure cycles, accompanied by a distinct shift of the pore volume peak toward larger pore sizes. These observations confirm that NaCl crystallization preferentially occupies smaller pores (<0.1 μm), consistent with earlier reports on NaCl deposition in cement mortar (0.01–0.08 μm)[27] and limestone (0.01–0.12 μm)[53]. Since gas diffusion primarily occurs in pores > 10^{-3} μm[54], the accumulation of salt crystals progressively impedes vapor transport in dry-cup tests, resulting in a systematic reduction of permeability coefficients (Fig. 3 and Table 4). In contrast, wet-cup tests revealed an opposing mechanism: deliquescence of salt crystals under high humidity alleviates pore blockage, while concurrent brine-vapor migration through interconnected pores enhances moisture transport efficiency, thereby increasing water vapor permeability coefficients (Fig. 3 and Table 5). This humidity-dependent dual behavior underscores the two roles of NaCl—pore occlusion by crystallization under low humidity (dry-cup) versus transport enhancement through deliquescence under high humidity (wet-cup).

For comparative analysis with immersion-based methods[35,46], specimens immersed in 2.39 wt% NaCl solution (simulating seawater salinity) for 48 h were also examined (Fig. 5f). The reduction in pore volume within the 0.02–0.12 μm range due to immersion was similar to that observed in specimens subjected to 7/14 salt spray cycles (Fig. 5a, b), suggesting comparable pore-filling mechanisms between salt spray deposition and salt solution immersion. This similarity persists despite differences in salt delivery (surface deposition vs. bulk infiltration), supporting the general applicability of NaCl-induced pore structure modifications in porous matrices.

Specific surface area, defined as the total surface area per unit mass of a material, encompasses both external and internal surfaces in porous systems, with its magnitude governed by pore morphology and surface characteristics. Together with pore volume distribution, it fundamentally defines a material's microstructure and governs its macroscopic properties[55,56]. To track pore structure evolution in cement mortar under salt spray exposure, cumulative pore volume and specific surface area were measured using mercury intrusion porosimetry (MIP) for reference specimens and specimens exposed to 7–35 salt spray cycles (Fig. 6). Reference specimens showed the highest values, with a cumulative pore volume of 0.069 m^3/g and a specific surface area of 5.218 m^2/g. Both parameters decreased progressively as exposure cycles increased—a trend attributed to the substantial filling of 0.02–0.12 μm pores by deposited NaCl crystals (Fig. 5), as corroborated by earlier analysis.

The reduction in specific surface area observed in salt-containing specimens arises from two principal mechanisms. First, partial filling of micropores by salt crystals converts them into denser solid structures, thereby diminishing the internal surface area. Second, unlike Na_2SO_4 crystals that typically form along pore walls, NaCl nucleates at liquid–gas interfaces and grows toward the pore walls, without covering the internal pore surface until contact is made[19,28,53,57]. Although crystallization increases the total internal surface area in absolute terms, it also raises the specimen mass. Given that dry NaCl crystals have a density of 2165 kg/m^3 at 23 °C under standard pressure[19]—higher than the measured density of cement mortar (2133 kg/m^3)—and considering the non-porous nature of NaCl relative to the porous mortar matrix, salt deposition ultimately reduces the specific surface area of the composite material.

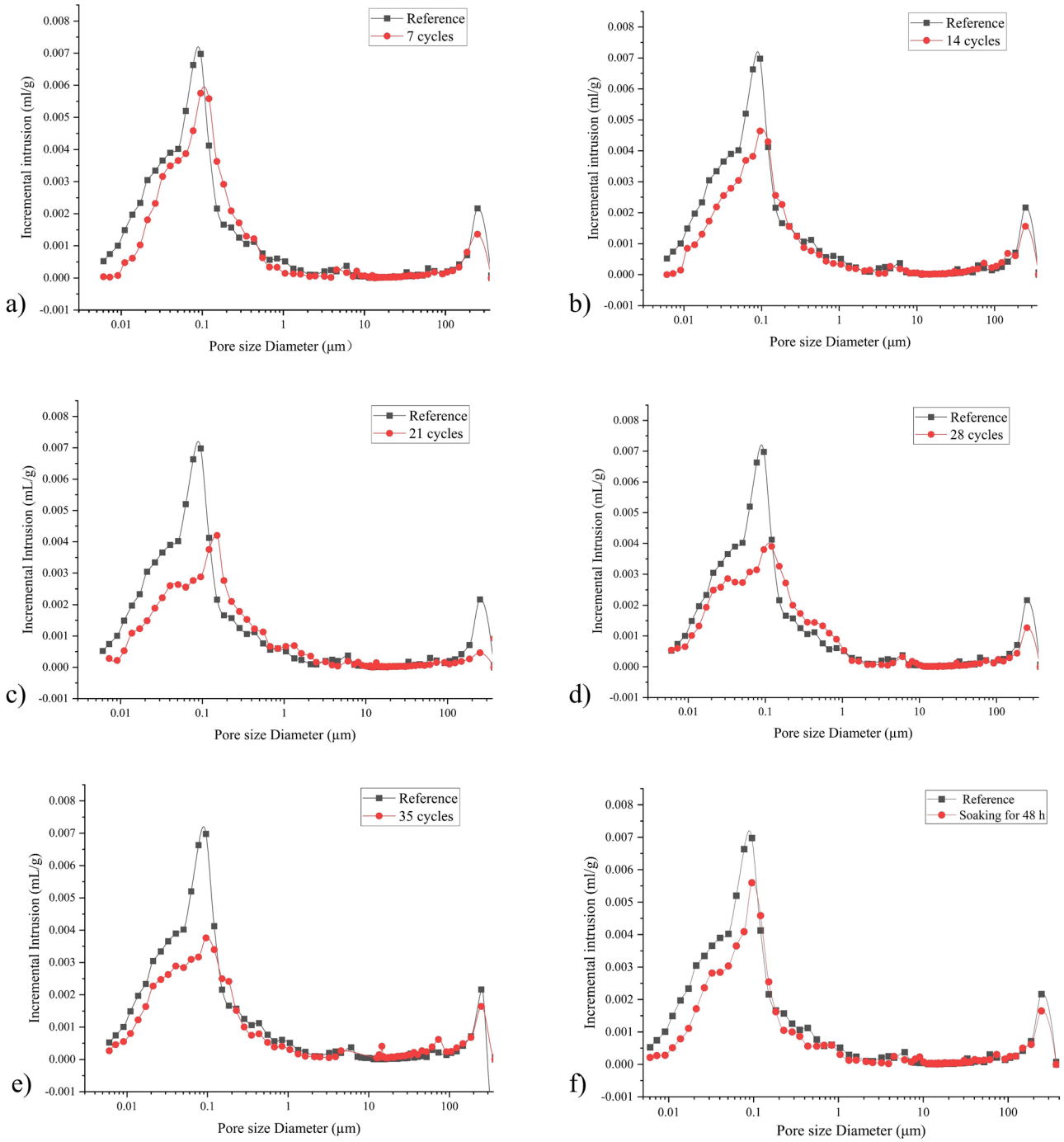

Fig. 5 | Pore size distribution of cement mortar with salt deposition (a–e: 7–35 salt spray cycles; f: 48 h salt solution immersion). The figure comprises six panels presenting mercury intrusion porosimetry (MIP) results. Panels **a**–**e** show the pore size distributions of cement mortar specimens after 7, 14, 21, 28, and 35 salt spray cycles, respectively, in comparison with reference specimens. Panel **f** presents the pore size distribution of specimens immersed in salt solution for 48 h, also compared with reference specimens. In all panels, black squares and curves represent the reference specimens, while red dots and curves represent the salt-exposed specimens. The results consistently show that salt deposition preferentially occupies pores in the 0.02–0.12 μm range across all exposure conditions.

It is noteworthy that although NaCl deposition reduces specific surface area (m^2/g), it increases the absolute external surface area per unit volume (m^2/m^3) within pore space. This extended interface enhances gas-solid contact, thereby raising flow resistance. As a result, the observed decrease in water vapor permeability with increasing salt content below 75% RH (Fig. 2, Tables 2 and 4), can be explained by the presence of undissolved salt crystals, which impede vapor transmission through surface adsorption mechanisms.

To visualize microstructural evolution under cyclic salt spray exposure, scanning electron microscopy (SEM) observations were performed on cement mortar specimens across all salt spray cycles (Fig. 7). After 7 cycles, cubic NaCl crystals densely covered the surface, resulting in noticeable surface roughening. By 14 cycles, crystal density increased, with particles exhibiting more irregular shapes and smaller sizes, forming thicker coatings. At 21 cycles, granular crystals transitioned to interconnected flake-like layers. After 28 cycles, cluster crystal aggregates developed, and by 35 cycles, salt had diffused inward into subsurface pores, with fine crystals adhering to larger molten clusters.

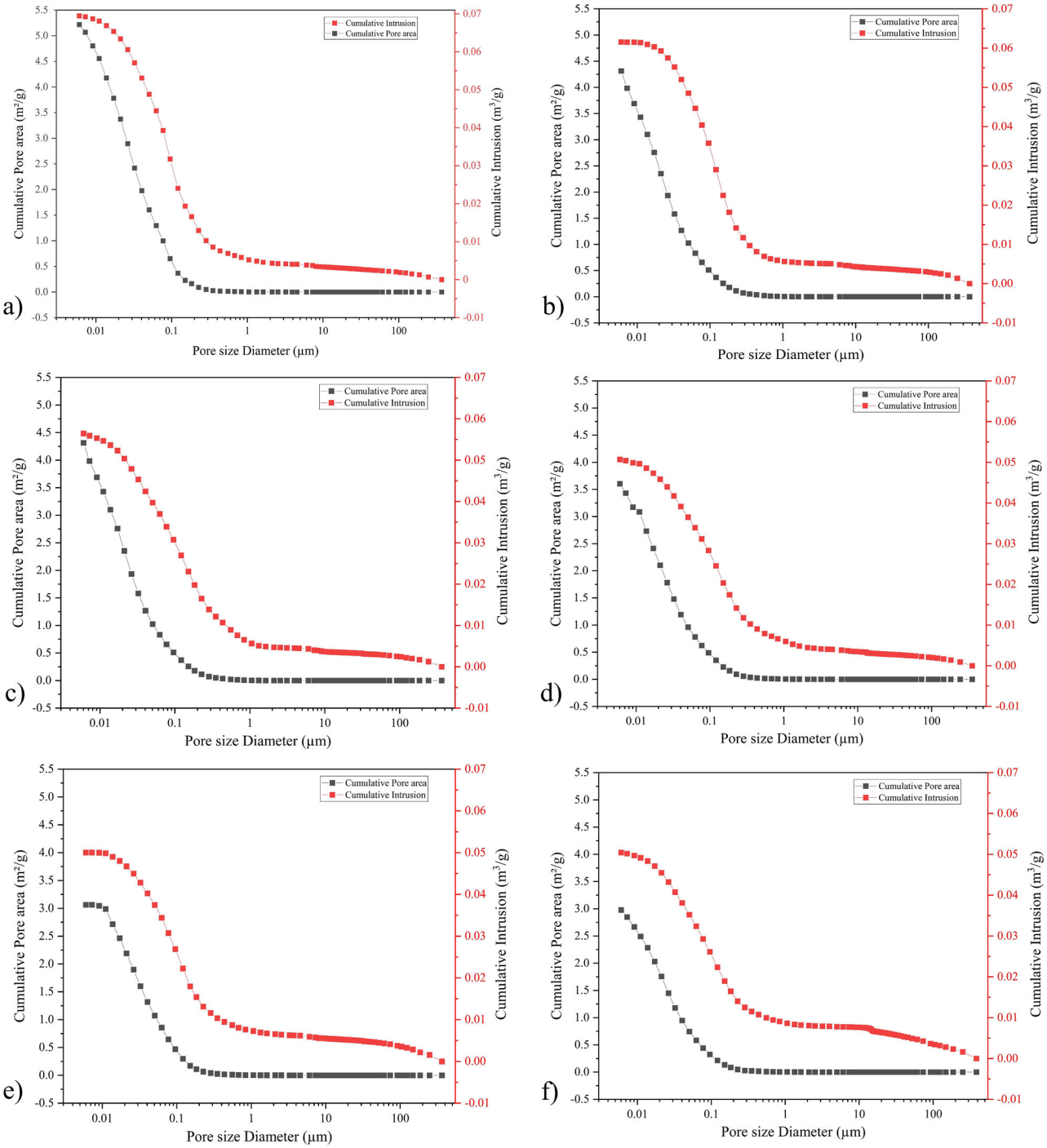

Fig. 6 | Cumulative pore volume and specific surface area of cement mortar subjected to varying salt spray cycles. The figure comprises six panels presenting mercury intrusion porosimetry (MIP) results. Panel **a** shows the cumulative intrusion and cumulative pore area of the reference specimens (0 cycles). Panels **b**–**f** present the corresponding results for specimens after 7, 14, 21, 28, and 35 salt spray cycles, respectively. In all panels, red squares and curves represent cumulative pore volume (right vertical axis), while black squares and curves represent cumulative pore area (left vertical axis). Comparison across the six panels clearly reveals the evolution of pore volume and specific surface area in cement mortar with increasing salt spray exposure.

Salt crystallization morphology and distribution evolve dynamically through repeated deposition, crystallization, dissolution, and redistribution during wet-dry cycling. Since water vapor transport occurs primarily through open surface pores, changes in near-surface pore density and connectivity critically influence vapor permeability. The observed progression—from sparse to dense coverage and from thin films to thick crystalline layers—demonstrates how NaCl deposition progressively occludes surface pores, reducing open porosity by 18–32% and thereby impeding vapor transport[19,30]. These microstructural transformations directly corroborate the 22–45% reduction in water vapor permeability coefficients measured via dry-cup tests (Fig. 3, Table 4), establishing a causal relationship between morphological evolution and macroscopic moisture transport properties.

To comprehensively evaluate microstructural changes in cement mortar induced by salt spray exposure, cross-sectional morphologies at different depths were examined and compared with reference specimens (Fig. 8). Reference samples (Ra–Rd) exhibited characteristic cementitious

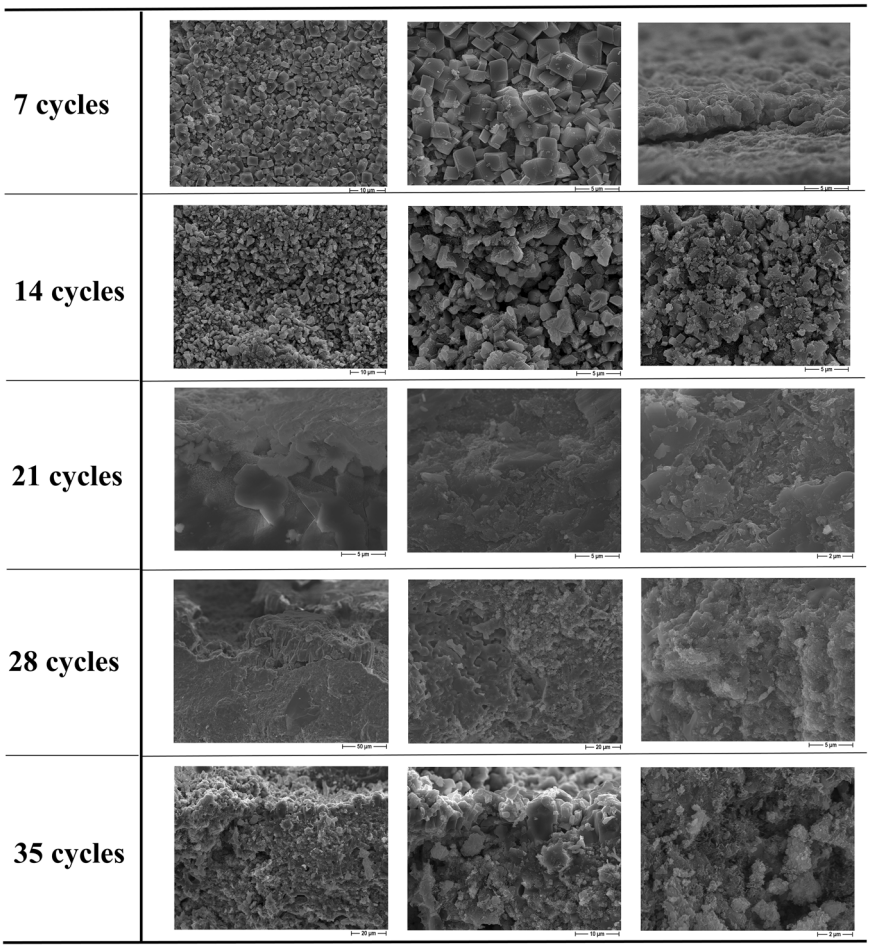

Fig. 7 | Surface salt crystallization morphology of cement mortar under varying salt spray cycles (SEM). The figure presents scanning electron microscopy (SEM) images showing the evolution of salt crystallization on cement mortar surfaces after 7–35 salt spray cycles. Specimens exposed to 7, 14, 21, 28, and 35 cycles are arranged in five rows from top to bottom, with each row containing three representative images at different magnifications or locations. Comparative observation across the panels reveals progressive changes in both the amount and morphology of surface salt crystals with increasing exposure cycles: from sparse, well-defined cubic crystals at early stages to denser, interconnected crystalline clusters and thicker coatings at later stages.

phases, including C-S-H gel networks, needle-like ettringite ($3CaO.Al_2O_3.3CaSO_4.32H_2O$), and rod/plate-shaped portlandite. After 7–14 salt spray cycles, localized but dense NaCl crystals formed within interfacial voids (Fig. 8 7a–14d). With further cycling (21–35 cycles), salt clusters proliferated, occluding fine pores while generating larger macropores with smoother surfaces (Fig. 8 21a–35d). These observations confirm that salt deposition modifies both surface and subsurface pore networks. NaCl migration operates through humidity-driven dissolution-recrystallization dynamics: under humid conditions, deliquescence enables brine infiltration into deep pores via wicking[29,30], while drying cycles drive internal brine toward shallow regions, culminating in recrystallization and pore architecture modification. The progressive accumulation of salt crystals corresponds to the persistent decrease in 0.02–0.12 μm pore volumes observed during salt spray testing (Fig. 5a–e). Moreover, higher salt content amplifies hygroscopic moisture uptake and liquid-phase transport under elevated humidity. Repeated crystallization and dissolution cycles continuously reshape the pore network, providing a mechanistic explanation for the contrasting water vapor permeability behaviors measured in dry- and wet-cup tests (Tables 4 and 5).

This study systematically investigated the evolution of water vapor permeability in cement mortar, a material representative of historic building fabric, under a coastal climate. The investigation integrated accelerated salt spray testing (35 cycles, 5% NaCl solution), dry-cup/wet-cup measurements, and microstructural characterization. The major findings are summarized as follows:

(1) Experiment results establish a critical humidity-regulated duality in salt-permeability interactions: below NaCl's 75% RH deliquescence threshold (~75% RH at 23 °C), salt contamination reduces water vapor permeability coefficients (δv) by up to 1.86×10^{-12} kg/(m s Pa) through crystalline pore occlusion; while above this threshold, δv increases by up to1.98×10^{-11} kg/(m s Pa) via deliquescence-induced brine films that facilitate moisture diffusion through connected liquid pathways. This phase-transition-driven reversal fundamentally dictates moisture transport behavior in salt spray environments.

(2) To quantify these mechanisms, we developed a generalized piecewise correction framework using quadratic polynomial regression. The model incorporates humidity-specific salt influence factors—$\eta_{\delta v} = (-2983.71C^2 + 59.12\,C + 0.68)$ for $\varphi \le 0.75$ and $\eta_{\delta v} = (6035.16C^2 - 28.26\,C + 1.51)$ for $\varphi > 0.75$ (where C is salt content in kg/kg)—which scale the baseline vapor permeability ($\delta_{v,\,r}$) to predict the behavior of salt-laden mortar. The established Eq. 9 comprehensively accounts for the coupled effects of salt content and ambient humidity on vapor permeability in porous materials, offering relatively direct and accurate input parameters for building hygrothermal simulations.

(3) Microstructural analyses (MIP/SEM) revealed progressive evolution of salt crystallization: initial surface-deposited cubic crystals (7–14 cycles) transition to interconnected subsurface clusters (21–35 cycles), preferentially occupying pores in 0.02–0.12 μm range and reducing near-surface porosity by 16–42%. This microstructural transformation directly explains the suppression of δv observed in dry-cup tests. Conversely, deliquescence-generated solution migration above 75% RH critically enhances moisture transport in wet-cup configurations, with salt redistribution depths exceeding 2 mm after prolonged exposure.

These findings provide a mechanistic framework for understanding moisture transport in porous materials under salt spray

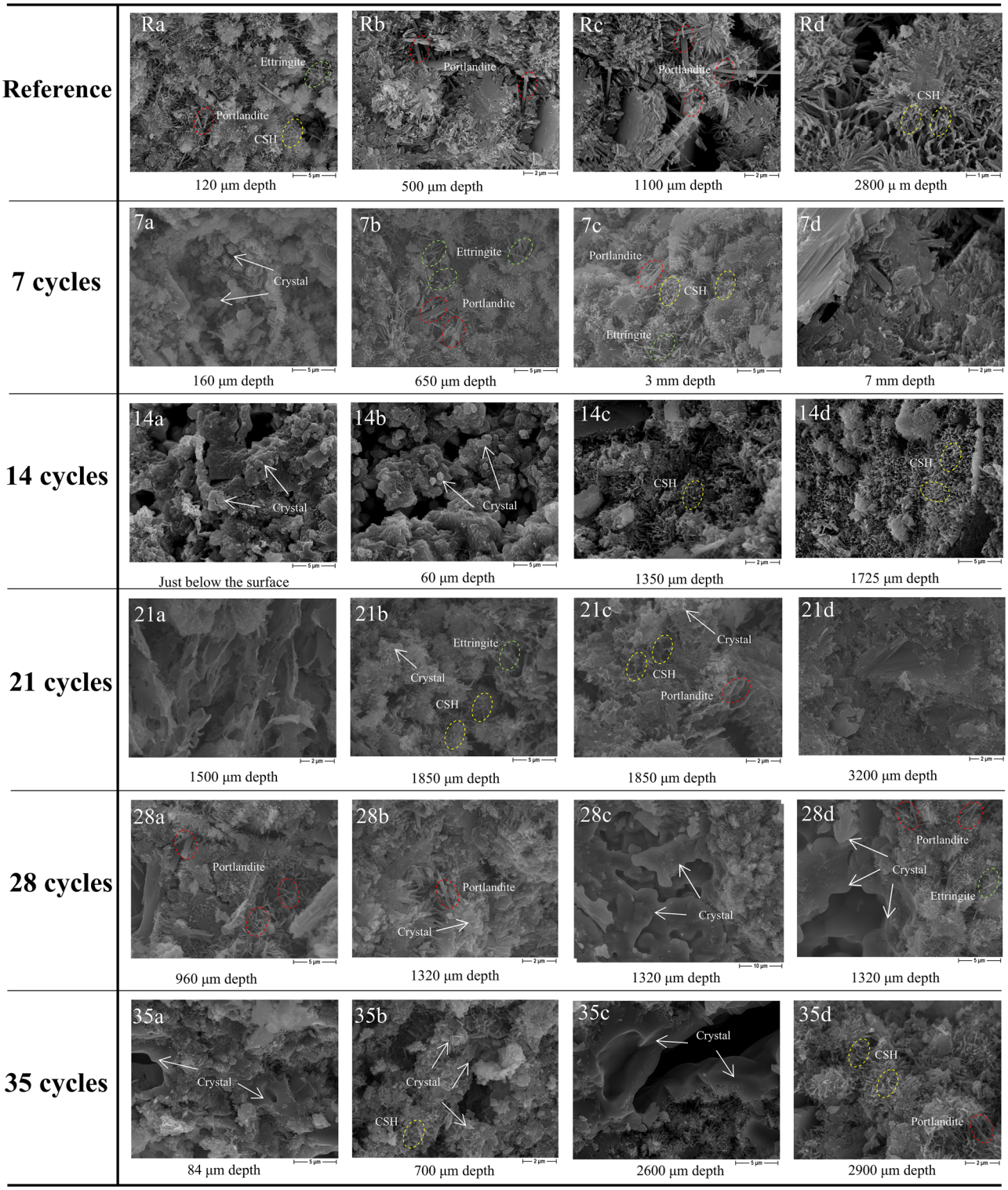

Fig. 8 | Internal morphology of cement mortar under varying salt spray cycles (SEM). The figure presents cross-sectional scanning electron microscopy (SEM) images illustrating the internal microstructure of cement mortar specimens. The first row (panels Ra–Rd) shows reference specimens (0 cycles) imaged at various depths or different magnifications. Rows 2–6 (each containing four panels a–d) correspond to specimens after 7, 14, 21, 28, and 35 salt spray cycles, respectively. To facilitate identification of key phases, the following annotations are used: red dashed ellipses indicate portlandite; yellow dashed ellipses indicate C–S–H gel; green dashed ellipses indicate ettringite; and white arrows indicate salt crystals.

deposition, enabling improved prediction of moisture-related parameters and physical properties for coastal built heritage. However, two limitations should be acknowledged. First, the experiments were conducted solely on cement mortar. Although most porous building materials—like cement mortar—do not chemically react with NaCl and undergo only physical changes, with moisture transport primarily governed by pore structure, the specific hygric behavior of other materials under salt spray deposition still requires rigorous experimental validation. Second, while NaCl is the predominant salt in seawater, accounting for approximately 69% of total seawater ions, the

effects of other marine salts on heritage building materials cannot be neglected. Future research will extend this framework to multi-salt systems and investigate the interaction mechanisms of mixed salts within porous materials, thereby providing further theoretical support for the development of conservation strategies for historic buildings and cultural heritage in coastal regions.

Data availability

The datasets generated and/or analyzed during the current study are not publicly available due to ongoing research, but are available from the corresponding author on reasonable request.

Received: 22 November 2025; Accepted: 11 April 2026;
Published online: 27 April 2026

References

1. Zhao, J. et al. Characterization of hygrothermal properties of two wood species—the impact of anisotropy on their thermal and moisture behaviors. *Constr. Build. Mater.* **398**, 132375 (2023).
2. d'Ambrosio Alfano, F. R., Palella, B. I. & Riccio, G. Moisture in historical buildings from causes to the application of specific diagnostic methodologies. *J. Cult. Herit.* **61**, 150–159 (2023).
3. Koronthalyova, O. Moisture storage capacity and microstructure of ceramic brick and autoclaved aerated concrete. *Constr. Build. Mater.* **25**, 879–885 (2011).
4. Pinheiro, V. R. F. et al. Evaluation of the influence of climatic changes on the degradation of the historic buildings. *Energy Build.* **323**, 114813 (2024).
5. Karoglou, M. et al. Monitoring of a historic building's masonry moisture content. *J. Build. Eng.* **104**, 112313 (2025).
6. Sheng, L. et al. Assessing the deterioration risk of polychrome clay sculptures based on the hygrothermal environment: a case study of Baosheng temple, China. *Case Stud. Constr. Mater.* **17**, e01287 (2022).
7. Gaylarde, C. C. et al. Metagenomic and morphological analysis of biodeteriogenic biofilms on historic stone buildings in the tropical north-east of Brazil. *Int. Biodeterior. Biodegrad.* **204**, 106143 (2025).
8. Blumberga, A. et al. Trilemma of historic buildings: smart district heating systems, bioeconomy and energy efficiency. *Energy* **186**, 115741 (2019).
9. Lubelli, B. et al. Influence of brick and mortar properties on bioreceptivity of masonry—results from experimental research. *Constr. Build. Mater.* **266**, 121036 (2021).
10. Jin, X. et al. From the coast to the interior: global economic evolution patterns and mechanisms. *Humanit. Soc. Sci. Commun.* **10**, 723 (2023).
11. He, F. et al. Offshore Island Connection Line: a new perspective of coastal urban development boundary simulation and multi-scenario prediction. *GISci. Remote Sens.* **59**, 801–821 (2022).
12. Cosby, A. G. et al. Accelerating growth of human coastal populations at the global and continent levels: 2000–2018. *Sci. Rep.* **14**, 22489 (2024).
13. Wei, G., Han, G.-S. & Lang, X. Cultural heritage site selection characteristics and the impact of the natural environment in Jinan city, China. *Sci. Rep.* **14**, 31038 (2024).
14. Hu, H. Climate and environmental dynamics: deciphering the distribution and vulnerability of world heritage sites in Europe. *J. Environ. Manag.* **392**, 126693 (2025).
15. Morillas, H. et al. The influence of marine environment on the conservation state of Built Heritage: an overview study. *Sci. Total Environ.* **745**, 140899 (2020).
16. Morillas, H. et al. Composition and porosity study of original and restoration materials included in a coastal historical construction. *Constr. Build. Mater.* **178**, 384–392 (2018).
17. Morillas, H. et al. Decay processes in buildings close to the sea induced by marine aerosol: salt depositions inside construction materials. *Sci. Total Environ.* **721**, 137687 (2020).
18. Koronthalyova, O. et al. Effect of presence of salt on hygric performance of ceramic bricks. *Transp. Porous Media* **107**, 667–682 (2015).
19. Todorović, J. & Janssen, H. The impact of salt pore clogging on the hygric properties of bricks. *Constr. Build. Mater.* **164**, 850–863 (2018).
20. Huang, D. et al. Diffusion behavior of chloride in coral aggregate concrete in marine salt-spray environment. *Constr. Build. Mater.* **316**, 125878 (2022).
21. Delgado, J. M. P. Q. et al. Salt damage and rising damp treatment in building structures. *Adv. Mater. Sci. Eng.* **2016**, 1–13 (2016).
22. Pozo-Antonio, J. S. Evolution of mechanical properties and drying shrinkage in lime-based and lime cement-based mortars with pure limestone aggregate. *Constr. Build. Mater.* **77**, 472–478 (2015).
23. Hendrickx, R. et al. Experimental investigation of the influence of precipitated salts on the liquid transport properties of brick using an organic fluid. In Salt Weathering on Buildings and Stone Sculptures (eds Ioannou, I. & Theodoridou, M.) (University of Cyprus, 2011).
24. Angeli, M. et al. Modification of the porous network by salt crystallization in experimentally weathered sedimentary stones. *Mater. Struct.* **41**, 1091–1108 (2008).
25. Lubelli, B., van Hees, R. P. J. & Groot, C. J. W. P. Sodium chloride crystallization in a "salt transporting" restoration plaster. *Cem. Concr. Res.* **36**, 1467–1474 (2006).
26. Koniorczyk, M. Salt transport and crystallization in non-isothermal, partially saturated porous materials considering ions interaction model. *Int. J. Heat Mass Transf.* **55**, 665–679 (2012).
27. Koniorczyk, M. & Gawin, D. Heat and moisture transport in porous building materials containing salt. *J. Build. Phys.* **31**, 279–300 (2008).
28. Espinosa-Marzal, R. M. & Scherer, G. W. Impact of in-pore salt crystallization on transport properties. *Environ. Earth Sci.* **69**, 2657–2669 (2013).
29. Pel, L., Huinink, H. & Kopinga, K. Salt transport and crystallization in porous building materials. *Magn. Reson. Imaging* **21**, 317–320 (2003).
30. Li, B. et al. Salt migration and capillary absorption characteristics of cement mortar partially immersed in NaCl solution. *J. Build. Eng.* **64**, 105605 (2023).
31. Li, B. et al. The hygric properties of cement mortar with salt spray deposition. *Constr. Build. Mater.* **449**, 138438 (2024).
32. Su, L. et al. Chloride diffusion behavior and microstructure of basalt–polypropylene hybrid fiber reinforced concrete in salt spray environment. *Constr. Build. Mater.* **324**, 126716 (2022).
33. Franzoni, E. et al. Effects of rising damp and salt crystallization cycles in FRCM-masonry interfacial debonding: towards an accelerated laboratory test method. *Constr. Build. Mater.* **175**, 225–238 (2018).
34. Pel, L., Huinink, H. & Kopinga, K. Ion transport and crystallization in inorganic building materials as studied by nuclear magnetic resonance. *Appl. Phys. Lett.* **81**, 2893–2895 (2002).
35. Bai, L. et al. Effect of salt on hygroscopic properties of cement mortar. *Constr. Build. Mater.* **305**, 124746 (2021).
36. Xie, Y. et al. Experimental study on the effect of salt on the water absorption characteristic of cement mortar. *J. Build. Eng.* **73**, 106693 (2023).
37. Petković, J. et al. Salt transport in plaster/substrate layers. *Mater. Struct.* **40**, 475 (2006).
38. Franzoni, E. et al. The role of mortar matrix in the bond behavior and salt crystallization resistance of FRCM applied to masonry. *Constr. Build. Mater.* **209**, 592–605 (2019).
39. ISO 12572: 2016(E). *Hygrothermal Performance of Building Materials and Products — Determination of Water Vapour Transmission Properties — Cup Method.* (International Organization for Standardization, Geneva, 2016).

40. BS EN 14147: 2003(E). *Natural Stone Test Methods — Determination of Resistance to Ageing by Salt Mist*. (British Standards Institution, London, 2003).
41. ASTM B117–2011(E) *Standard Practice for Operating Salt Spray (Fog) Apparatus*. (ASTM International, West Conshohocken, PA, 2011).
42. ISO 15148: 2002(E). *Hygrothermal Performance of Building Materials and Products. Determination of Water Absorption Coefficient by Partial Immersion.* (International Organization for Standardization, Geneva, 2002).
43. ISO 21466: 2019(E). *Microbeam Analysis — Scanning Electron Microscopy — Method for Evaluating Critical Dimensions by CD-SEM.* (International Organization for Standardization, Geneva, 2019).
44. ISO 15901-1: 2005(E). *Evaluation of Pore Size Distribution and Porosimetry of Solid Materials by Mercury Porosimetry and Gas Adsorption.* (International Organization for Standardization, Geneva, 2005).
45. Li, B. et al. Fitting equations for the sorption isotherms of cement mortar with salt spray deposition. *Front. Archit. Res.* **15**, 872–891 (2025).
46. Xie, Y., Xie, J.-C. & Bai, L. Experimental study on the effect of salt on vapor migration in cement mortar. *Build. Energy Effic.* **49**, 45–51 (2021). (in Chinese).
47. Méndez-Bermúdez, J. G. et al. Composition and temperature dependence of the dielectric constant of 1-propanol/water mixtures: experiment and molecular dynamics simulations. *J. Mol. Liq.* **219**, 354–358 (2016).
48. Franke, L. & Grabau, J. The influence of salt content on the drying behavior of brick. In Conservation of Historic Brick Structures: Case Studies and Reports of Research (eds Baer, N. S., Fitz, S. & Livingston, R. A.) 59–68 (Donhead, 1998).
49. Hendrickx, R., Roels, S., De Clercq, H. & Vanhellemont, Y. Experimental determination of liquid transport properties on salt-contaminated porous stone. In *12th International Conference on Durability of Building Materials and Components* 125–132 (Porto, Portugal, 2011).
50. Charola, A. E. Salts in the deterioration of porous materials: an overview. *J. Am. Inst. Conserv.* **39**, 327 (2000).
51. Rovnanikova, P. Environmental pollution effects on other building materials. *Trends Genet. Tig* **10**, 225–226 (2007).
52. Lubelli, B., van Hees, R. P. J. & Brocken, H. J. P. Experimental research on hygroscopic behaviour of porous specimens contaminated with salts. *Constr. Build. Mater.* **18**, 339–348 (2004).
53. Rodriguez-Navarro, C. & Doehne, E. Salt weathering: influence of evaporation rate, supersaturation and crystallization pattern. *Earth Surf. Process. Landf.* **24**, 191–209 (1999).
54. Lubelli, B. Sodium chloride damage to porous building materials. PhD thesis, Delft University of Technology. https://resolver.tudelft.nl/uuid:c8d72659-ca2f-4a82-aa5c-b4a39b6daaf8 (2006).
55. Sibiryakov, B., Leite, L. W. B. & Sibiriakov, E. Porosity, specific surface area and permeability in porous media. *J. Appl. Geophys.* **186**, 104261 (2021).
56. Ghasemi, Y., Emborg, M. & Cwirzen, A. Exploring the relation between the flow of mortar and specific surface area of its constituents. *Constr. Build. Mater.* **211**, 492–501 (2019).
57. Benavente, D. et al. Role of pore structure in salt crystallisation in unsaturated porous stone. *J. Cryst. Growth* **260**, 532–544 (2004).

Acknowledgements

The authors gratefully acknowledge the SISCON Laboratory at Politecnico di Torino for supporting the experimental activities. This work was supported by the Natural Science Foundation of Xinjiang Uygur Autonomous Region (Grant No. 2025D01C12) and the National Natural Science Foundation of China (Grant Nos. 51938006, 52468004).

Author contributions

Bing Li: Writing—original draft, investigation, and formal analysis. Xiyang Dai: Data curation and visualization. Simin He: Validation. Saierjiang Halike: Funding acquisition. Feng Shi: Methodology. Jean-Marc Tulliani: Resources and investigation; Junsong Wang: Project administration. Qinglin Meng: Funding acquisition and supervision.

Competing interests

The authors declare no competing interests.

Additional information

Correspondence and requests for materials should be addressed to Bing Li or Saierjiang Halike.